JOURNAL OF GEOPHYSICAL RESEARCH, VOL. 106, NO. A5, PAGES 8343–8356, MAY 1, 2001

Experimental investigations on photoelectric and triboelectric charging of dust

A. A. Sickafoose, J. E. Colwell, M. Horányi, and S. Robertson

Laboratory for Atmospheric and Space Physics, University of Colorado, Boulder, Colorado

Abstract. Experiments are performed pertaining to the charging of single dust particles in space due to three effects: (1) photoemission, (2) the collection of electrons from a photoemissive surface, and (3) triboelectric charging. The particles tested are 90–106 μm in diameter and include JSC-1 (lunar regolith simulant) and JSC-Mars-1 (Martian regolith simulant). Isolated conducting grains (Zn, Cu, and graphite) illuminated by ultraviolet light reach a positive equilibrium floating potential (a few volts) that depends upon the work function of the particle. Conducting grains dropped past a photoemitting surface attain a negative floating potential for which the sum of the emitted and collected currents is zero. Nonconducting grains (glass, SiC, and the regolith simulants) have a large initial triboelectric charging potential (up to $\pm$15 V) with a distribution approximately centered on zero. The nonconducting grains are weak photoemitters, and they attain a negative floating potential when dropped past a photoemitting surface. Our experimental results show that for silicate planetary regolith analogs, triboelectric charging may be the dominant charging process and will therefore play an important role in the subsequent behavior of dust grains released from planetary surfaces.

1. Introduction

Dust grains suspended above the lunar surface have been observed on multiple occasions. A horizon glow roughly 1 m above the surface of the Moon was detected by Surveyor 5, 6, and 7 (and perhaps 1) [*Rennilson and Criswell*, 1974] and more recently by the Clementine spacecraft [*Zook et al*., 1995]. At spacecraft sunrise, Apollo astronauts observed high-altitude streaks due to light scattered from particles extending from the lunar surface to above the spacecraft [*Zook and McCoy*, 1991]. The Lunar Ejecta and Meteorite Experiment (LEAM) deployed by Apollo 17 also detected evidence for horizontal dust transport on the surface of the Moon at sunrise and sunset [*Berg et al*., 1975]. Dust dynamics such as these are thought to be the result of the interaction between charged dust particles and a photoelectron layer above the lunar surface. In this paper we present results of experiments on the charging of isolated grains from photoemission and from the photoelectron layer above a surface illuminated by UV.

Understanding the charging of dust particles on or near surfaces in space is necessary to quantify and characterize the transport and levitation of lunar regolith particles in the photoelectron sheath. In addition, dusty regoliths are produced on the surfaces of virtually all airless bodies in the solar system through ongoing bombardment by the interplanetary micrometeoroid flux. Dust is launched off the surface of asteroids by impacts into asteroidal regolith of large ejecta blocks and by collisions between asteroids. Whether these particles escape the asteroid's relatively weak gravity or return to the surface depends not only on the ejecta velocity but also on the dynamics of the charged dust particles in the photoelectron sheath just above the asteroid surface [*Lee*, 1996]. The dust rings of the giant planets are created by the loss of dust particles from the regoliths of the larger parent moons and moonlets [e.g., *Burns et al*., 1999; *Horányi et al*., 1992; *Showalter and Cuzzi*, 1993; *Colwell and Esposito*, 1990a, 1990b]. Electromagnetic forces help sculpt these dust rings and may also play a role in the liberation of dust particles from the surfaces of the parent bodies, such as that which occurs in the spokes of Saturn's rings [*Nitter et al*., 1998; *Goertz*, 1989]. Additionally, electromagnetic dust levitation and transport may be important processes on Mercury [*Ip*, 1986], comets [*Mendis et al*., 1981], planetary satellites, planetesimals, and Mars [*Grard*, 1995]. In particular, small grains lifted off the Martian surface by saltation or turbulent flows in the near-surface boundary layer could have their dynamics affected by the photoelectron layer. The depth and distribution of the dusty regolith on planetary bodies can be measured by infrared observations. Thus, understanding dust charging and transport on and above planetary surfaces is crucial for interpreting remote sensing data and analyzing the evolution of planetary surfaces and planetary dust rings.

Theoretical work has been done on the characteristics of photoelectron layers, the trapping of dust in a sheath, and one-dimensional horizontal dust transport within a sheath [*Nitter et al*., 1998; *Nitter and Havnes*, 1992; *Pelizzari and Criswell*, 1978; *Singer and Walker*, 1962a, 1962b]. Laboratory experiments have been done on photoemission from satellite surface materials and the resulting charging potentials [*Feuerbacher and Fitton*, 1972; *Diebold et al*., 1988]. Experiments have also demonstrated that lunar dust simulant can be electrostatically levitated by photoelectric charging [*Doe et al*., 1994]. This work confirms the plausibility of photoelectric charging to explain observed dust transport phenomena. However, an experiment has not been performed which measures the charge on a single dust particle in a photoelectron sheath.

We have constructed an experiment to investigate the charging of dust particles from photoemission and from electron collection within a UV-induced photoelectron sheath. The dust particles used are 90–106 μm in diameter and are com-

Paper number 2000JA000364.
0148-0227/01/2000JA000364$09.00

posed of zinc, copper, graphite, JSC-1 (lunar regolith simulant), JSC-Mars-1 (Martian regolith simulant), glass, or SiC. In section 2 we provide a background on charging processes in space. In section 3 we describe the experimental apparatus, the grain materials, and the techniques for sample preparation and charge measurement. In section 4 we present photoelectric charging measurements for isolated conducting grains and for conducting grains dropped past a photoemitting surface, and we investigate the charging of the regolith simulants. The regolith simulant charging is compared with that of two nonconductors: glass and SiC. The data are discussed and conclusions are drawn in section 5.

2. Background

Objects in space charge to a floating potential determined by the balance between the charging currents in the local plasma environment. The primary charging currents are due to electron and ion collection, photoemission, and secondary electron emission. Charge accumulation continues until the increased potential results in the sum of the locally modified currents being zero. This equilibrium value of the potential is referred to as the floating potential.

Within a planetary magnetosphere, magnetically trapped charged particles and secondary electrons usually dominate charging. If the plasma electron energy distribution has a cutoff at maximum energy $E_{\max}$, the equilibrium charging potential on a dust particle will be $-E_{\max}/e$, where e is the elementary charge. The ion charging current is usually much smaller than the electron current, owing to the smaller ion thermal velocity. The effect of a small added ion current is a floating potential slightly more positive than $-E_{\max}/e$, which allows just enough electron collection to cancel the flux of ions. For distributions of particle energies, each charging current is found by an appropriate integral over the distribution of emitted or collected particles, and the floating potential has the value which makes the sum of the integrals zero.

In interplanetary space, where the plasma density is that of the tenuous solar wind, photoelectric charging usually exceeds plasma charging. Electrons will be lost owing to photoemission, and objects will reach a positive floating potential dependent on the energy of the incoming photons and the photoelectric work function of the surface. In a steady state the photoelectrons can form a sheath near the surface of large bodies, such as the Moon.

The experiments we have performed deal with three specific cases of dust charging: the charge on isolated grains due to photoemission, the charge on grains due to interaction with a photoelectron sheath surrounding a larger body, and triboelectric charging.

2.1. Charging of Grains Due to Photoemission

In order for the charging currents to balance for isolated grains in interplanetary space, photoemitting grains must attain a positive floating potential. If the spectrum of illumination has a short-wavelength cutoff at wavelength $\lambda_{\min}$, the maximum energy of photons is $hc/\lambda_{\min}$, where h is Planck's constant and c is the speed of light. The maximum energy of the emitted electrons is $(hc/\lambda_{\min} - \phi_g)$, where ϕ_g is the photoelectric work function of the grain in units of energy. The grain then charges approximately to the positive potential $(hc/\lambda_{\min} - \phi_g)/e$. The charge on the grain is determined by $Q = CV$, where V is the particle potential and C is the grain capacitance. For a spherical grain of radius r_g, $C = 4\pi\varepsilon_0 r_g$, and the maximum charge on the grain is

$$Q = 4\pi\varepsilon_0 r_g \left(\frac{hc}{\lambda_{\min}} - \phi_g \right) \Big/ e \tag{1}$$

[*Wood*, 1981; *Rosenberg et al*., 1996]. A more accurate value is obtained by finding the potential at which the photoemission and electron collection are equal (see section 4.1). If there is no short-wavelength cutoff in the spectrum, the photoemission current is found from an integral that includes only the highest-energy electrons which escape from the confining potential well.

2.2. Charging of Grains Above Surfaces

Photoemission can also occur from the surfaces of moons and small planets having insufficient atmosphere to absorb UV. In the absence of other charging processes these bodies will become positively charged, as would a small grain. In equilibrium, nearly all emitted photoelectrons will be returned to the surface. These outbound and inbound electrons form a photoelectron sheath, or layer, above the surface. Typical sheath dimensions are tens of centimeters to 2 m at distances of 1 AU [*Walbridge*, 1973].

In the case of thermionic emission like that from a heated cathode of a vacuum tube, the electron energy distribution is a single-sided Maxwellian, and the nature of the sheath has been investigated in detail [*Suits*, 1961a, 1961b]. The density and potential as a function of distance are found by solving simultaneously Poisson's equation and the Vlasov equation. The structure of a photoelectron sheath has also been found for several other model distribution functions [*Singer and Walker*, 1962a; *Grard and Tunaley*, 1971; *Walbridge*, 1973]. Regardless of the energy distribution, the photoelectron layer has a shielding distance that is the analog of the Debye length for charge-neutral plasmas. The length scale can be written as

$$\lambda_e = \left(A \frac{\varepsilon_0 K_{\text{avg}}}{ne^2} \right)^{1/2}, \tag{2}$$

where K_{avg} is the average electron energy, n is the electron density, and A is a coefficient near unity which depends upon the details of the electron energy distribution function.

The photoelectron sheath above the lunar surface was first discussed in detail by *Singer and Walker* [1962a, 1962b]. They argued that the Moon attains a floating potential at which the flux of electrons from the solar wind is balanced by the loss of a small fraction of the electrons from the sheath. Later work made use of data from the lunar surface and returned soil samples to create models that are more constrained. For example, *Walbridge* [1973] found a mean photoelectron energy of 2 eV, an electron density of 4×10^3 cm^{-3}, and a shielding distance of 13 cm for the lunar photoelectron sheath. *Willis et al*. [1973] found that lunar samples had a lower photoelectric yield than was assumed by Walbridge, and they calculated a density at the lunar surface of 130 cm^{-3} with a shielding distance of 78 cm. Additionally, measurements of the energy distribution of returning electrons made by the Charged Particle Lunar Environment Experiment [*Reasoner and Burke*, 1973] showed that the surface potential may reach 200 V when the Moon is in the magnetotail and shielded from the solar wind. In the presence of the solar wind, however, the surface potential was too low to have a clear signature in these data.

Dust released from the surface of the Moon or other pho-

toemitting bodies will collect electrons from the sheath. If the dust grains and the surface have similar rates of photoemission, the greater emitting area of the surface will result in the charging current for the grain being dominated by the collection of electrons from the sheath. If there is a short-wavelength cutoff to the spectrum and the surface can be characterized by a single value of the work function, then the maximum energy of photoelectrons in the sheath is $(hc/\lambda_{\min} - \phi_s)$, where ϕ_s is the work function of the photoemitting surface. For a grain that does not photoemit, the maximum charging potential while in the sheath will be

$$Q = -4\pi\varepsilon_0 r_g\left(\frac{hc}{\lambda_{\min}} - \phi_s\right)\Big/ e. \tag{3}$$

For a photoemitting grain within the sheath a less negative charging potential is reached at which the current of collected sheath electrons cancels the photoemission.

The grain potential may, in fact, be positive if the grain is sufficiently far from the surface for the collection of sheath electrons to be reduced. This change in polarity is likely to occur several screening distances from the surface. The loss of photoelectrons from the lunar surface results in a sheath electric field pointing upward. Therefore the change in sign of the dust grain charge with distance means that the more distant positive particles might be levitated, depending upon the relative strengths of the electric force and gravity. The positively charged particles more distant from the surface are thought to be responsible for the lunar horizon glow.

It is not sufficient for dust levitation that the electric and gravitational forces should cancel; the equilibrium must also be stable. Stability occurs when the upward electric force falls more quickly than the gravitational force does. This is nearly always the case for dust within the sheath of larger objects because the scale height of the electron sheath is usually much less than the radius of the object. The relative importance of the electrostatic force on dust is greater in lower-gravity environments such as asteroids, planetary rings, and small planetary satellites. The appearance of a levitated layer also requires a mechanism for raising the grains into the region of the stable equilibrium and their having a sufficient time to reach the equilibrium charge [*Nitter et al*., 1998].

2.3. Triboelectric Charging

Triboelectric charging refers to the transfer of charge via contact. This process occurs for similar materials in contact as well as dissimilar materials. Unlike a contact potential difference, which occurs for two dissimilar metals and is usually of the order of 1 V, triboelectric charging accumulates and may result in potential differences of kilovolts. Substances have been arranged into triboelectric series based on their tendency to become positive or negative, but there is no first-principles theory for triboelectricity as there is for the contact potential. The relevant properties of the materials are more likely to be those of the surface than those of the bulk.

Triboelectric charging is rarely discussed for grains at rest but is frequently invoked as a mechanism for charging of windblown grains. This is because rubbing increases the surface charge by increasing the fraction of the area in contact [cf. *Lowell and Rose-Innes*, 1980; *Harper*, 1967]. Strong electric fields, which may arise from triboelectricity, have been observed near dust devils [*Freier*, 1960] and may occur on Mars [*Melnik and Parrot*, 1998; *Farrell et al*., 1999]. Spectacular lightning discharges observed in volcanic plumes may also result from triboelectric charging of dust grains [*Gilbert et al*., 1991; *Anderson et al*., 1965].

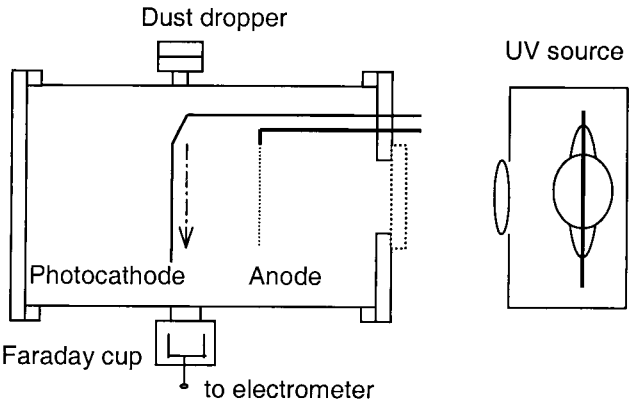

Figure 1. Schematic diagram of the experimental setup. The dust (dash-dotted arrow) falls from a dropper at the top of the chamber. The dust falls into a Faraday cup below the chamber, which measures the amount of charge. For experiments using a photoelectron sheath the dust falls past the photocathode. The photocathode is removed for studies on the photoemission of isolated grains. The anode is used to characterize the photoelectron sheath and is removed for dust charging experiments.

3. Experimental Techniques

3.1. Apparatus

The experimental apparatus shown in Figure 1 is a modification of a device used earlier for studying the charging of dust particles by plasma [*Walch et al*., 1994, 1995; *Robertson*, 1995], including lunar dust [*Horányi et al*., 1998]. The apparatus consists of an aluminum vacuum chamber 30 cm in diameter and 30 cm long evacuated to 4×10^{-7} torr by a diffusion pump. The interior of the chamber has a stainless steel liner to reduce photoemission and secondary electron emission from the walls. Stainless steel has a much lower photoelectric yield than aluminum for photons with energies less than 6 eV [*Feuerbacher and Fitton*, 1972]. Particles are dropped through the vacuum chamber from a dust dropper at the top and are collected in a Faraday cup at the bottom. The dropper contains a metal plate with a hole through which grains drop when the plate is agitated by a pulse to an electromagnet. The amplitude of the pulses is adjusted so that in most cases, grains drop individually. The Faraday cup is connected to a sensitive electrometer, and the height of the pulses is calibrated to give the charge on the grains. In cases where several grains drop at once, the pulses have a more complex shape and are rejected (Figure 2). The electrical noise in the circuit corresponds to roughly $5 \times 10^3\ e$, and the threshold for peak detection is set at $\pm 2 \times 10^4\ e$ to prevent the detection of noise peaks.

Three types of experiments are performed which require different configurations of the apparatus. For investigating triboelectric charging, the dust particles are dropped through a vacuum into the Faraday cup with no illumination. In this case the charges on the grains are the values the particles have when they leave the dropper. For studying photoelectric charging, the grains are illuminated by an arc lamp, and they become charged as a result of photoemission. Lastly, for investigating

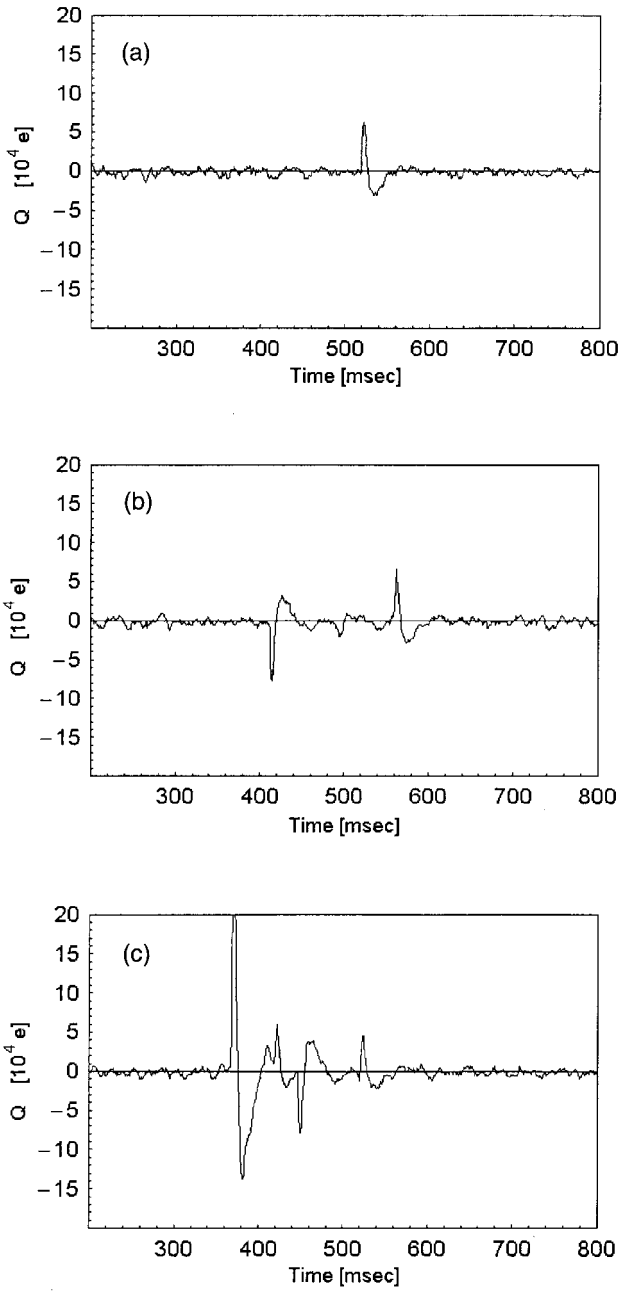

Figure 2. Oscillograms of signals from grains entering the Faraday cup. The vertical scale indicates the charge. The time delay is the time of flight through the chamber. (a) A typical waveform for the detection of a single dust grain. (b) A waveform for the detection of multiple grains. In this case, two separate grain charges are apparent. (c) A waveform for the detection of a dust clump. Only charge detections that match the form of Figure 2a are recorded in these experiments.

the charging of grains within a sheath, a photoemitting surface is placed vertically within the vacuum chamber and illuminated by the arc lamp. In this case, grains become charged negatively by the collection of photoelectrons emitted from the surface or positively by their own photoemission, depending upon the relative strengths of the two charging processes.

Grains of seven different materials are used in the study. The conducting materials are zinc, copper, and graphite, for which there are tabulated work functions [*Michaelson*, 1977]. These are chosen to span a range of photoelectric yields from relatively high (zinc) to low (graphite). The nonconductors are glass and SiC. The regolith materials are JSC-1, a lunar surface simulant, and JSC-Mars-1, a Mars surface simulant. The chemical composition, mineralogy, and particle size distribution of JSC-1 fall within the ranges of lunar mare soil samples [*McKay et al.*, 1994]. Likewise, JSC-Mars-1 approximates the reflectance spectrum, mineralogy, chemical composition, grain size, porosity, density, and magnetic properties of the oxidized soil of Mars [*Allen et al.*, 1998].

All dust samples are obtained in granular form, spanning a large range of particle sizes. These are dry sieved into size fractions using standard methods. Grains are used which have passed through square openings of 106 μm and have not passed openings measuring 90 μm. The dust particles are a variety of shapes, as seen in microphotographs (Figure 3). After being sieved, samples are stored in a vacuum for degassing. The capacitance of a spherical grain with a radius of 49 μm is 5.4 fF, thus we expect a charge of $\sim 3.4 \times 10^4$ electrons per volt of charging potential. The need to resolve the charge on the grains prevents the use of smaller particles. In addition, for particles smaller than ~ 20 μm, adhesion of grains results in the dropping of clumps rather than individual particles.

Illumination is provided by a 1 kW Hg-Xe arc lamp having a quartz envelope with an $f/1.0$ quartz collimating lens. From data provided by the manufacturer of the lamp system, we have calculated that $\sim 12\%$ of the energy from the lamp appears in the beam from the collimator. A few percent of this has a wavelength sufficiently short to cause photoemission, with $hc/\lambda_{\min} \approx 6.03$ eV. Commercial 30-W deuterium lamps with MgF_2 windows have a larger fraction of their spectrum in the ultraviolet. Direct comparisons of the photoemission created by the arc lamp and a deuterium lamp, however, show that the arc lamp provides an order of magnitude more photoemission.

A photoelectron sheath is created by placing a metal plate within the vacuum chamber and illuminating it with the arc lamp. This photocathode is oriented vertically so that the falling grains pass parallel to, and $\sim$1–2 cm from, the surface. Several metals of low work function were tried as candidate materials (Table 1). Zn was used initially, but the strong illumination heated the surface to the point of sublimation, which resulted in coating of the vacuum window. Hf and Zr have the lowest work functions of nonradioactive and nonreactive refractory metals. Of these, Zr is found to have the highest photoelectric yield in our experiment. Therefore the photocathode used in these experiments is a 12.5-cm diameter disk cut from zirconium foil. The Zr plate is illuminated in a central region 10 cm in diameter to minimize electron losses from the edge. The emission from a fresh Zr surface is ~ 38 μA, but after several hours of illumination the mean emission is ~ 20 μA. When the emission falls below this point, the surface is renewed by cleaning in diluted phosphoric acid.

3.2. Characterization of the Photoelectron Sheath

Modeling the charge on dust within a sheath requires knowledge of the photoelectron density and energy distribution function. These characteristics are found by the retarding potential method in which the current from the photocathode is measured as a function of its potential relative to an adjacent surface. For this measurement a 15-cm square grid of closely spaced ($\sim$1 mm) Ni wires is placed parallel to and a few centimeters from the photocathode (Figure 1), and the illumination passes through these grid wires. Ni (work function

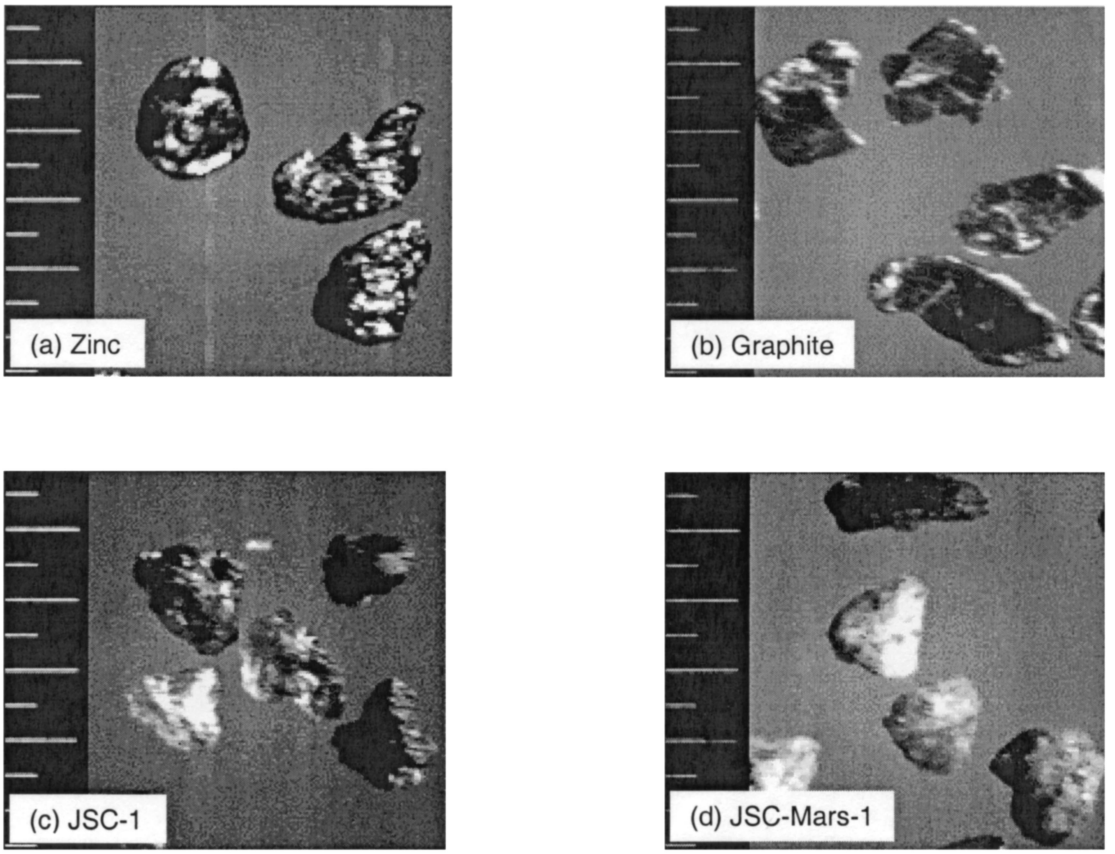

Figure 3. Microphotographs of (a) zinc, (b) graphite, (c) JSC-1, and (d) JSC-Mars-1 dust particles. The displayed scale is 50 μm per small division.

$\phi_{Ni} = 5.15$ eV) has a negligible photoelectric yield; thus emission from the grid wires does not perturb the measurements. Stray electrons are further suppressed by biasing the grid to -4.5 V, repelling any photoelectrons from the walls. The emission current from the Zr plate as a function of the bias potential is shown in Figure 4a. There is no significant current when the photocathode is several volts more positive than the Ni grid, indicating that stray electrons are suppressed. For these data the intensity of the lamp is reduced such that the maximum emission from the photocathode is 2 μA. At this low level of emission the space charge of the electrons is not sufficient to alter the shape of the current-voltage characteristic. The derivative of the characteristic, Figure 4b, is the electron energy distribution function $F(E)$, where E is the electron energy perpendicular to the photocathode surface. This distribution is well approximated by the normalized κ distribution used by *Mendis and Rosenberg* [1994]. A least squares fit to the data has the energy distribution

$$F(E) = D\,\frac{\Gamma(\kappa+1)}{[K_{avg}(2\kappa-3)]^{3/2}\Gamma(\kappa-1/2)} \cdot \left[1+\frac{2(E-E_0)^2}{K_{avg}(2\kappa-3)}\right]^{-\kappa-1}, \quad (4)$$

with the spectral index $\kappa = 2.31$, the average electron energy $K_{avg} = 1.42$ eV, and constants E_0 and D. The fraction of the total current from the photoelectron sheath collected by the grain as a function of its potential V, Figure 4c, is found by integrating the fitted κ distribution. The current from the sheath to the grain is discussed further in section 4.1.

The voltage axis in Figure 4a has an undetermined zero point because of the contact potential difference between the Zr surface and the Ni grid. The recorded voltage difference is that between copper wires connected to these surfaces. The potential in the vacuum immediately above the photocathode is more positive than the interior of the chamber due to the difference in the work functions of the materials. If there were no contact potential, the reduction of the current should begin when the cathode-anode potential is zero. In Figure 4a the current reduction is observed to occur at approximately -1 V because this value is required to eliminate the potential difference in the vacuum above the surfaces. This shift corresponds approximately to the difference between the work functions of Zr ($\phi_{Zn} = 4.05$ eV) and Ni ($\phi_{Ni} = 5.15$ eV).

Although well approximated by a normalized κ distribution,

Table 1. Photoelectric Currents Measured From Various Photocathode Materials

Metal	Work Function,[a] eV	Melting Point, °C	Maximum Photoelectric Yield, μA cm^{-2}
Zn	4.33	419.5	0.055
Ti	4.33	1668	0.061
Hf	3.9	2222	0.318
Zr	4.05	1852	0.483

[a]*Michaelson* [1977].

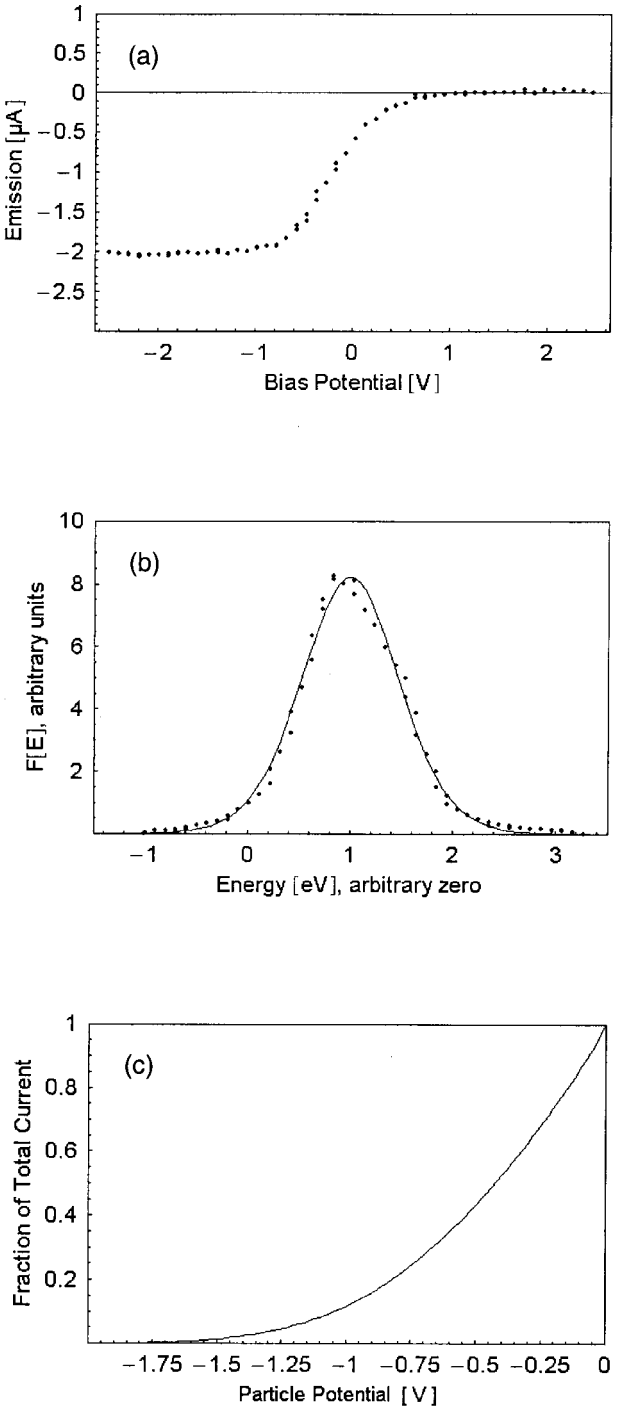

Figure 4. (a) Photocurrent from the cathode as a function of the bias potential. (b) The electron energy distribution perpendicular to the plate, obtained from the derivative of the curve in Figure 4a. The solid line is a least squares fit to the data using the κ distribution given in equation (4). (c) The fraction of total current to the grain from the sheath as a function of grain potential, calculated by equation (7) and integrating the κ distribution.

the electron energy distribution can also be modeled as an inverted parabola with small wings at the extremities. There should be no electrons with negative energies or with energies greater than the difference between the work function and the energy of the most energetic photons (6.03 eV). Therefore the wings of the distribution can be explained by small patches of material having a work function different from that of the substrate. This supposition is supported by the observation that the wings are much larger if the grid and photocathode are not cleaned in acid. An inverted parabola fit to the distribution with the wings removed has intercepts spaced in energy by 1.96 eV, in excellent agreement with the difference between the work function of Zr and the maximum photon energy (1.98 eV). The peak of the distribution in Figure 4b indicates a mean energy of ~1.1 eV, which corresponds to a mean velocity of emission of 6.2×10^5 m s^{-1}. This mean energy is slightly less than the average energy from the κ distribution fit because the wings are eliminated. For a typical photoemission current of 20 μA from the 10-cm illuminated region of the Zr plate (corresponding to a current density of ~0.255 μA cm^{-2}), the density of emitted photoelectrons is 2.5×10^4 cm^{-3}. This density is doubled when the surface is at the floating potential which returns the emitted electrons to the surface. The height above the emitting surface the photoelectrons can reach when their motion is controlled solely by electrostatic forces is defined by (2) with $A = 2/3$ [*Grard*, 1995; *Grard and Tunaley*, 1971]. Given the measured mean photoelectron energy and the doubled electron density for the sheath in our experiment, the shielding distance is $\lambda_e \approx 4$ cm.

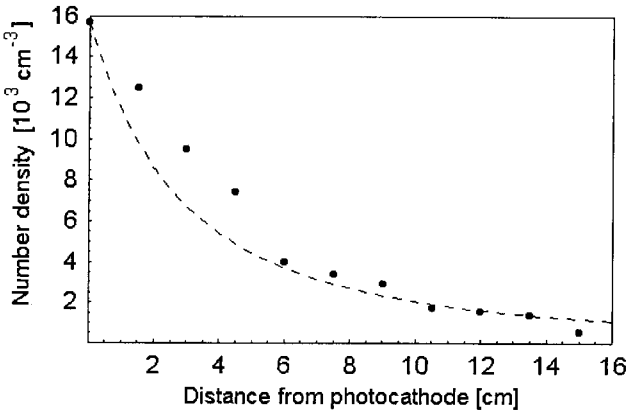

Figure 5. The photoelectron density as a function of distance from the surface of the photocathode. The data points are from a simulation of the photoelectron sheath made with the two-dimensional particle-in-cell code XOOPIC. The dotted line corresponds to the one-dimensional theoretical model given in equation (5).

The calculated photoelectron sheath characteristics are based on one-dimensional theoretical models. Our photocathode, however, has a transverse dimension of 12.5 cm, which is not much larger than the calculated sheath thickness of ~4 cm. The limited size of the photocathode may result in the sheath thickness and number density being less than that given by the model. This effect is investigated by using the two-dimensional particle-in-cell code XOOPIC [*Verboncoeur et al.*, 1995]. A cylindrical chamber is modeled with conducting boundaries at −1 V, the contact potential difference between Zr and stainless steel. The photocathode is modeled as a thermionic emitter with $1/2\ k_B T$ adjusted to match the measured mean photoelectron energy in the axial direction of 1.1 eV. Figure 5 shows the decay of the electron density with distance from the photocathode for this simulation. The XOOPIC data points

are compared to the electron density, n, as a function of distance from the photoemitter, z, for a Maxwellian velocity distribution [*Grard and Tunaley*, 1971]

$$n(z) = n_0\left[1 + \frac{z}{\sqrt{2}\,\lambda_e}\right]^{-2}, \tag{5}$$

where n_0 is the electron number density at $z = 0$. Figure 5 shows that the calculation from the one-dimensional model is in approximate agreement with the two-dimensional simulation. Because of the maximum energy cutoff for photoelectrons, the Maxwellian model overestimates the number of electrons at several scale heights from the surface. Therefore the electron density in the experiments may fall more quickly than that in (5). Section 4.3 discusses this in more detail. Investigation of the sheath by simple wire probes and emissive probes was unsuccessful owing to the low photoelectron density.

4. Experiments

4.1. Charging of Conducting Grains

The experiments are performed using homogeneous conducting materials with known properties (zinc, copper, and graphite) in order to facilitate comparison to theory and to confirm proper operation of the experimental apparatus. Positive charges are measured on these particles dropped through UV illumination, indicating a loss of electrons by photoemission. In the absence of illumination there are no detection events, indicating that the particles leave the dropper with a charge less (in absolute value) than the threshold of $2 \times 10^4\,e$, which corresponds to a charging potential of $\leq|\pm 0.6$ V|.

The grains are illuminated for a sufficient time to attain the equilibrium charging potential during photoemission experiments. The maximum charging time, dt, is found from the relationship between the current and the particle potential $I = C\,dV/dt$, or

$$dt = \frac{4\pi\varepsilon_0 r_g\,dV}{I}. \tag{6}$$

In this case the maximum photocurrent from the grain $I_g = J_g(V = 0)\pi r_g^2$, where $J_g(V = 0)$ is the current density due to photoemission from a particle at zero potential, C is the capacitance of a spherical grain having radius r_g, and dV is the maximum potential on a dust particle. Using the measured current density for zinc from Table 1 as $J_g(V = 0)$ and $dV = (hc/\lambda_{\min} - \phi_{\mathrm{Zn}}) = 1.70$ V, we find a charging time of 2.2 ms. This charging time is much smaller than the time to fall through the area of illumination (70 ms). The photoelectron yields of copper and graphite particles are not measured in our experiment. However, data for the least emissive material, graphite, indicate that the yield should not be lower than zinc by more than an order of magnitude [*Feuerbacher and Fitton*, 1972]. Thus copper and graphite also have sufficient time to reach the equilibrium charging potential.

Histograms of the charge due to photoemission on 100 grains of each conducting dust material are shown in Figure 6. Each histogram is fitted to a Gaussian distribution, $f(x) = B \exp[-(x - \mu)^2/2\sigma^2]$, where B is a constant, μ is the mean of the charging data, and σ is the standard deviation. The resulting least squares Gaussian fits to the data are shown as the solid lines in Figure 6. Owing to the threshold for detection, no grains are recorded at low charge values when, in fact, there are possibly grains having that charge. Thus the fits are made only to those charge values for which grains have been detected in order to avoid a bias from the threshold for detection.

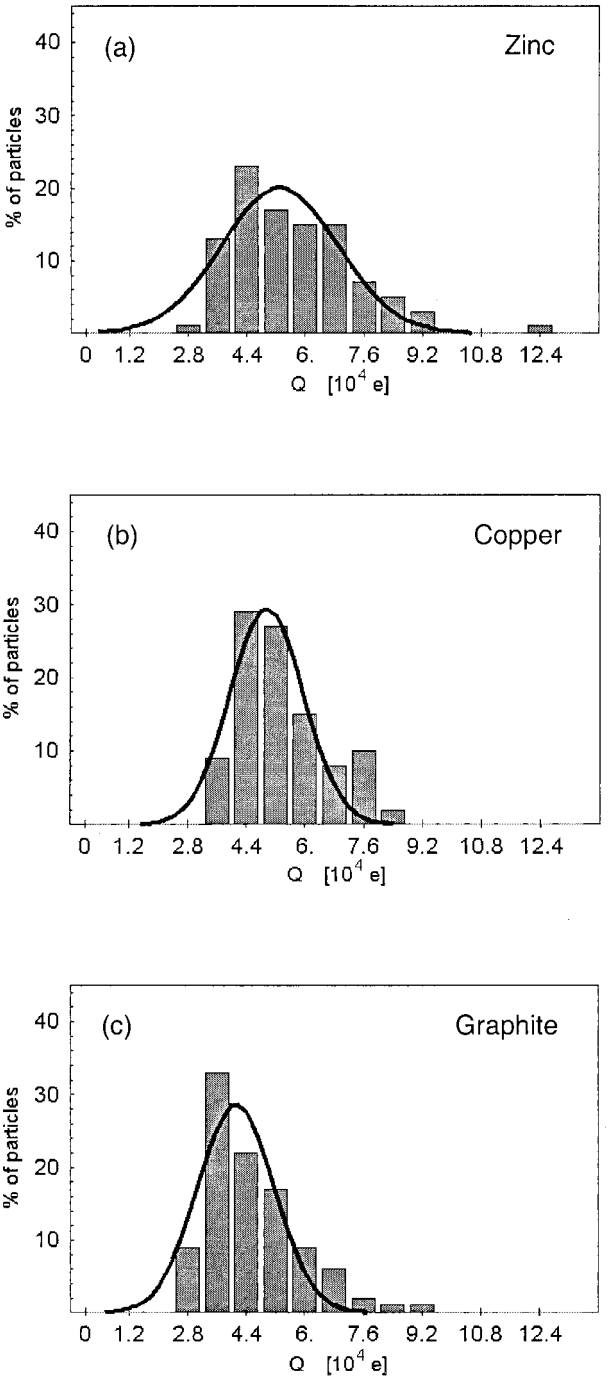

Figure 6. Charge distributions for 100 grains of (a) zinc, (b) copper, and (c) graphite, where grains were exposed to the arc lamp. Each material loses electrons owing to photoemission. The bin size is $0.8 \times 10^4\,e$, and zero is labeled for reference. The solid line is a least squares Gaussian fit to the data.

The measured charges due to photoemission (mean charge ± standard deviation from the Gaussian fits) are listed in Table 2. The observed charges for the materials show the expected variation with the tabulated photoelectric work functions. Zinc, with the lowest work function, has the highest

Table 2. Photoemission Data for Conducting Grains

Material	Work Function,[a] eV	Measured Charge, $10^4\ e$	Calculated Charge, $10^4\ e$
Zinc	4.33	5.3 ± 1.7	5.8 ± 0.6
Copper	4.65	5.0 ± 1.0	4.7 ± 0.5
Graphite	5.0	4.1 ± 1.2	3.5 ± 0.5

[a]*Michaelson* [1977].

charge ($5.3 \times 10^4\ e$). Graphite, with the highest work function, has the lowest charge ($4.1 \times 10^4\ e$). The measured charges can be compared to the values calculated from (1), where $hc/\lambda_{\min} = 6.03$ eV. This equation gives a single value; however, the measurements have a range of values as a result of electrical noise in the circuitry and the spread in grain sizes and shapes. We have obtained a mean and standard deviation for the calculated charge by using a power law particle size distribution within the range passed by the sieves and by the addition of measured circuit noise. The peaks of the measured distributions are all within 18% of the calculated charge peaks. The noise level is $5 \times 10^3\ e$, and the spread in size based upon the sieves is 5%. By allowing another 5% for the uncertainty in the capacitance due to shape, the spread in measurements is taken into account. The greatest spread in charge values occurs for graphite, which has the greatest variation in shape (Figure 3). In addition, there may be a slight systematic error from the samples not having exactly the work functions given in the tables.

For grain charging within a photoelectron sheath the equilibrium charge is determined by the balance between the loss of electrons from photoemission and the collection of electrons from the sheath. For grains which do not photoemit we expect a negative charging potential of −1.98 V, determined by the energy of the most energetic photoelectron. From (3) this corresponds to a maximum charge of $-6.8 \times 10^4\ e$. Photoemitting grains will have a potential that is some fraction of this value, which equalizes the loss of photoelectrons and the collection of electrons from the sheath.

The measured electron density above the photocathode is sufficient for grains to reach their equilibrium charging potential while falling through the sheath. The charging time is again found from (6). In this case the maximum photocurrent is $I_s = J_s(V = 0)4\pi r_g^2$, where $J_s(V = 0)$ is the current density from the sheath to a particle at zero potential. Using the measured current density for the zirconium photocathode from Table 1 as $J_s(V = 0)$ and $dV = (hc/\lambda_{\min} - \phi_{Zr}) = 1.98$ V, the calculated charging time is less than 1 ms. This is significantly shorter than the time to fall through the sheath of ~70 ms.

The current collected by a particle as a function of its potential is found by integrating over the distribution of incident electrons. For a monoenergetic electron distribution of energy E, the electron current collected by a grain with a potential V is $I_s(V) = J_s(V = 0)A_g[1 + eV/E]$ for $eV > -E$, where $J_s(V = 0)$ is the current density to a surface at zero potential and $A_g = 4\pi r_g^2$ is the surface area of the grain. For a distribution of electrons, $F(E)$, the collected current is then

$$I_s(V) = J_s(V = 0)A_g \int_{-eV}^{K_{\max}} F(E)\left[1 + \frac{eV}{E}\right] dE, \qquad (7)$$

where $K_{\max}$ is the maximum electron energy and $F(E)$ is normalized to unity [*Sickafoose et al.*, 2000]. In order to calculate the current to a grain, the κ distribution fit to the measured electron energy distribution given by (4) is used as $F(E)$. The dimensionless integral in (7) represents the fraction of the maximum current collected by a grain. The resulting fraction of the maximum current collected by a grain as a function of its potential V is plotted in Figure 4c.

Equilibrium is reached when the current due to the collection of electrons from the sheath equals the loss of electrons due to photoemission; therefore equilibrium is obtained when $I_s(V) = I_g(V)$. The emission from a particle at negative potential is given by $I_g(V) = J_g(V = 0)\pi r_g^2$, where πr_g^2 is the illuminated surface area of the grain. Thus the equilibrium condition is met when the dimensionless integral in (7) has value $J_g(V = 0)/4J_s(V = 0)$. Given the current densities for a Zn grain and the Zr photocathode (Table 1), the fraction of the total current collected is 0.03, which occurs at a potential of roughly 0.68 $K_{\max}$ or −1.34 V ($-4.6 \times 10^4\ e$).

Measurements of the charge on conducting grains dropped through the sheath are shown in Figure 7. Gaussian distributions are fit to the data, and the mean charges and standard deviations are listed Table 3. The mean measured charge for Zn particles is $-4.3 \times 10^4\ e$. This value is 7% less than the charge estimated using the measured current densities. This slight discrepancy is most likely due to the particle being dropped at a distance of 1–2 cm from the photocathode, whereas the current densities used are those measured at the surface. The calculated charges for copper and graphite particles are dependent on the photocurrent from those materials, which was not measured. Hence, in Table 3 there is no calculated value for the equilibrium charge on grains of copper or graphite. The measured charge is the same, to within the experimental uncertainty, for each of the conducting materials. This occurs because the charging potential is determined primarily by the photoelectron energy and is only weakly dependent upon grain photoemission.

4.2. Charging of Nonconducting Grains

Experiments with the regolith simulants produce the result that the grains have a significant charge upon leaving the dropper. This charge is assumed to be triboelectric. Triboelectric charging occurs for both conducting and nonconducting grains; thus the absence of this charge on the conductors is likely to have been a result of the charge being conducted to the ground before the grains are dropped. To clarify the importance of grain conductivity, measurements are made on two nonconductors in addition to the regolith simulants: glass and SiC. The glass is in the form of hollow microballoons, and the SiC is a powdered abrasive.

Histograms of the charge measured without illumination on the nonconducting materials are shown in Figure 8. The parameters of the fitted Gaussian distributions are listed in Table 4. The triboelectric charge distributions are significantly broader than those from photoelectric charging and are approximately centered on zero. For example, SiC particles have a charge distribution centered at $-0.6 \times 10^4\ e$ with a standard deviation of $4.9 \times 10^4\ e$. This corresponds to a charging voltage of −0.18 ± 1.44 V. The triboelectric charge distribution for glass is broader than that of SiC, with a mean charging potential of 1.35 (± 2.17) V. The charge distribution for JSC-1 grains is broader still, having a mean charging potential of −0.32 (± 2.38) V. JSC-Mars-1 particles have the broadest charge distri-

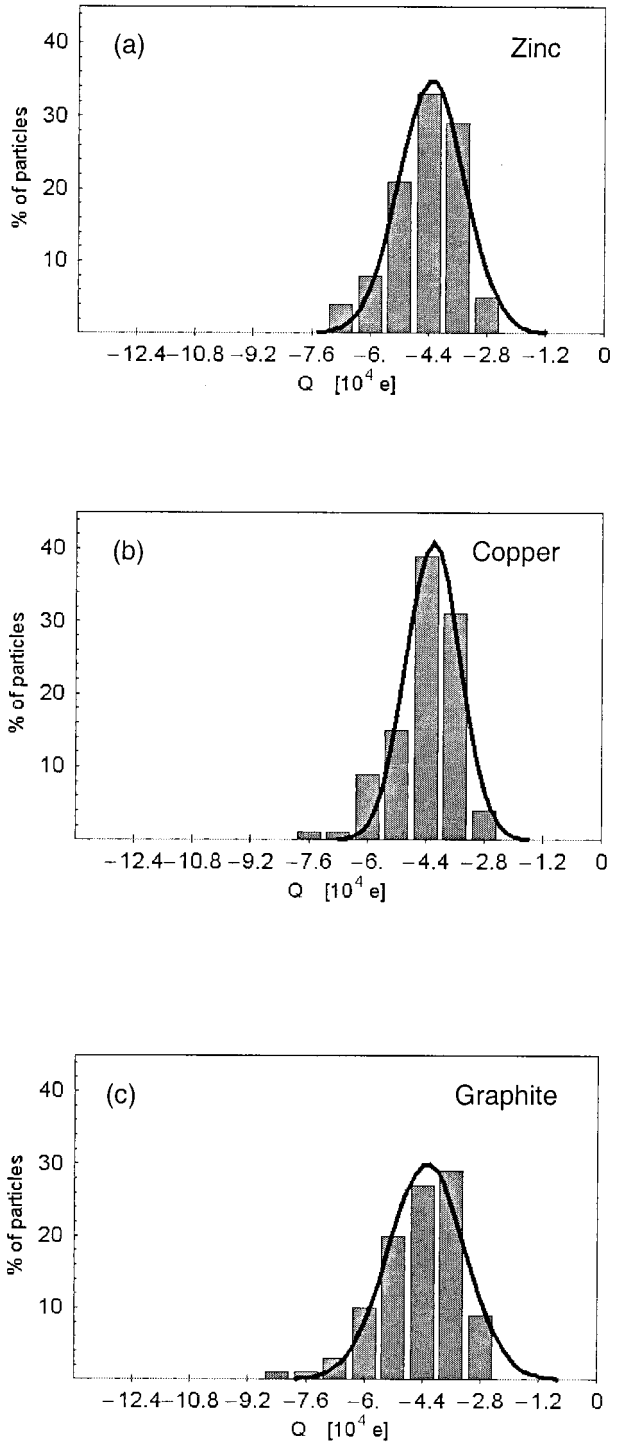

Figure 7. Charge distributions for 100 grains of (a) zinc, (b) copper, and (c) graphite, where grains fell through the photoelectron sheath. Each material gains electrons from the sheath. The bin size is 0.8×10^4 e, and zero is labeled for reference. The solid line is a least squares Gaussian fit to the data.

bution of all materials tested, with a mean charging potential of 2.12 ($\pm$ 6.71) V. In addition, charges of up to $\pm 52.0 \times 10^4$ e (corresponding to charging potentials of ± 15 V) are detected on single particles of JSC-Mars-1. Visual inspection of the regolith simulants shows that JSC-Mars-1 is composed of grains of different colors while JSC-1 grains appear uniform in color. This may indicate that the JSC-Mars-1 is more heterogeneous, which could account for the larger spread in triboelectric charge. However, the uniform color of the JSC-1 may be due to a surface coating of very fine (micron-sized) dust particles on the surfaces of the larger grains.

Table 3. Sheath Charging Data for Conducting Grains[a]

Material	Calculated Charge, 10^4 e	Measured Charge, 10^4 e
Zinc	-4.6 ± 0.4	-4.3 ± 0.9
Copper	NA	-4.2 ± 0.7
Graphite	NA	-4.3 ± 1.1

[a]NA, not available.

The triboelectric charging of glass in contact with metal is of order 10^{-5} C m^{-2} [*Lowell and Rose-Innes*, 1980]. Using this value, we can obtain an estimate for the triboelectric charge due to the contact between a glass microballoon and the dust dropper. Assuming the area in projection of a single particle is $\pi r_g^2 \approx 7000$ μm^2, the resulting charge on a particle is 7×10^{-14} C or 44×10^4 e. This is roughly a factor of 10 higher than the average charge measured on a glass particle. The disparity can be partially explained by the assumed charging value being for flat areas placed in contact, neglecting the effect of surface roughness on actual contact area. The calculation nevertheless demonstrates that triboelectricity is sufficient to explain the observed level of charge.

The charging of nonconducting grains due to photoemission is complicated by their initial triboelectric charge. Charge histograms for the nonconducting grains that have fallen through UV illumination are shown in Figure 9. The average charges and standard deviations for these materials are listed in Table 4. Those grains with triboelectric potential more positive than approximately -2 V will have all photoelectrons returned to the surface and thus have no change in their initial charge state. The rightmost histogram bars corresponding to charge $>8 \times 10^4$ e (2.35 V) indeed appear to be generally unchanged by UV illumination (compare Figure 8).

Those grains with an initially small negative charge will lose electrons by photoemission when exposed to UV. This reduction is easily seen in the histogram for SiC but is not obvious for the other materials. This suggests that SiC has the greatest photoelectric yield of the nonconductors. The fact that the negative grains retain most of their charge indicates that the photoelectric yield of all the nonconductors is too small for the equilibrium charge to be reached.

The charging of nonconducting grains in the photoelectron sheath is also affected by the initial triboelectric charge. The grains with initial charge more negative than -1.98 V receive no sheath electrons but may lose some charge owing to photoemission. Positive grains will collect electrons from the sheath and approach equilibrium charging potentials near -1.98 V, similar to the conducting grains. Indeed, the charging data for this situation, Figure 10, show almost no grains with a positive charge. The initially positive grains appear in the first histogram bar to the left of the origin because they have accumulated a small negative charge within the sheath. Further inspection of the histograms shows that SiC has fewer grains with charge $<-12 \times 10^4$ e (-3.5 V) than it had previously, indicating a loss of electrons by photoemission from very negatively charged grains. The most negative parts of the histograms for the more weakly emitting materials are largely un-

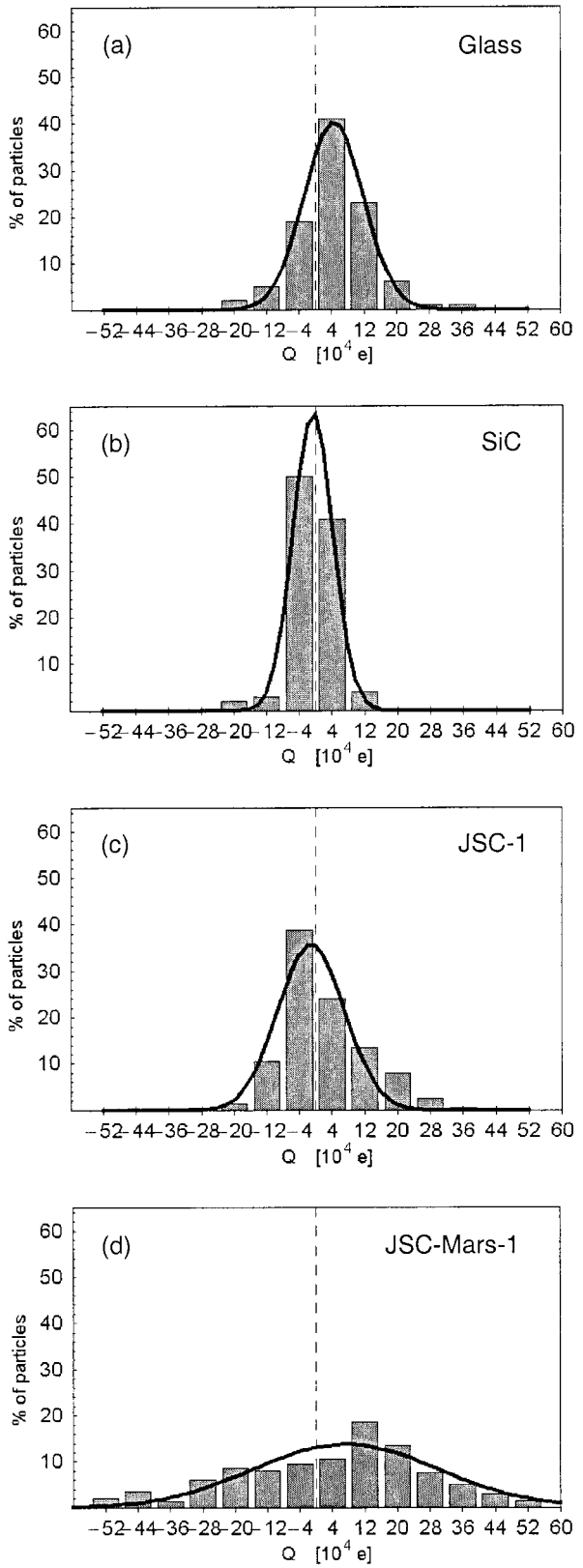

Figure 8. Triboelectric charge distributions for 100 grains of (a) glass and (b) SiC, and 200 grains of (c) JSC-1 and (d) JSC-Mars-1. The bin size is $8.0 \times 10^4\ e$, an order of magnitude larger than the histogram bins for the conducting materials. The dashed line represents zero, the boundary between gaining and losing electrons. The solid line is a least squares Gaussian fit to the data.

Table 4. Charge Data for Nonconducting Grains

Material	Triboelectric Charge, $10^4\ e$	Average Photoemission Charge, $10^4\ e$	Average Charge From Electron Collection Within the Sheath, $10^4\ e$
Glass	4.6 ± 7.4	7.2 ± 10.5	-6.7 ± 3.5
SiC	-0.6 ± 4.9	1.9 ± 4.7	-2.3 ± 5.4
JSC-1	-1.1 ± 8.1	-1.6 ± 12.6	-6.9 ± 3.8
JSC-Mars-1	7.2 ± 22.8	-0.6 ± 18.8	-16.6 ± 14.3

changed. The absence of the positive grains and a broad distribution of negative grains result in the standard deviation of the charge being a relatively large fraction of the mean. These values are listed in Table 4.

4.3. Charge Versus Distance From the Photocathode

As discussed in section 2.1, levitation of grains above the lunar surface is thought to occur for positively charged grains. The equilibrium charging potential within the sheath depends upon the distance of the grain from the surface. At greater distances the grain charging will be dominated by photoemission from the grain, and the equilibrium charge will be positive rather than negative. The charging potential as a function of distance from the photocathode is investigated by dropping zinc grains past the photoemitter with the distance from the surface being increased after each 100 drops (Figure 11). Charges between $-2.0 \times 10^4\ e$ and $2.0 \times 10^4\ e$ cannot be detected owing to noise in the circuit; therefore this region in the plot is shaded.

The particles falling short distances from the photocathode become negatively charged. With increasing distance, however, the relative importance of photoemission increases, and the equilibrium charge is more positive. At a sufficient distance the charging current from sheath electrons is merely a small perturbation upon the equilibrium charge from photoemission. The transition occurs at a distance of ~4.5–7 cm from the photocathode. Owing to the competing effects of photoemission and collection of electrons from the sheath, the charge on particles in this region is below the detection threshold. Thus the transition region is represented by a vertically shaded area in Figure 11.

In order to compare these measurements with theory, the current to a particle as a function of both particle potential and distance from the plate is calculated. An appropriate expression for the current to a particle in the sheath can be found by assuming a Maxwellian velocity distribution for the electrons released from the photocathode. The most important difference between this assumption and the experiments is the lack of high-energy photoelectrons due to the cutoff in photon energy in the experiments. The current is a function of photoelectron density, and density as a function of distance from the photocathode assuming a Maxwellian initial velocity distribution has been previously calculated by *Grard and Tunaley* [1971]. Therefore the current as a function of distance from the photocathode is a combination of (5) and (7),

$$I_s(V, z) = J_s(V = 0) A_g \left[1 + \frac{z}{\sqrt{2}\,\lambda_e} \right]^{-2} \cdot \int_{-eV}^{K_{\max}} F(E) \left[1 + \frac{eV}{E} \right] dE. \quad (8)$$

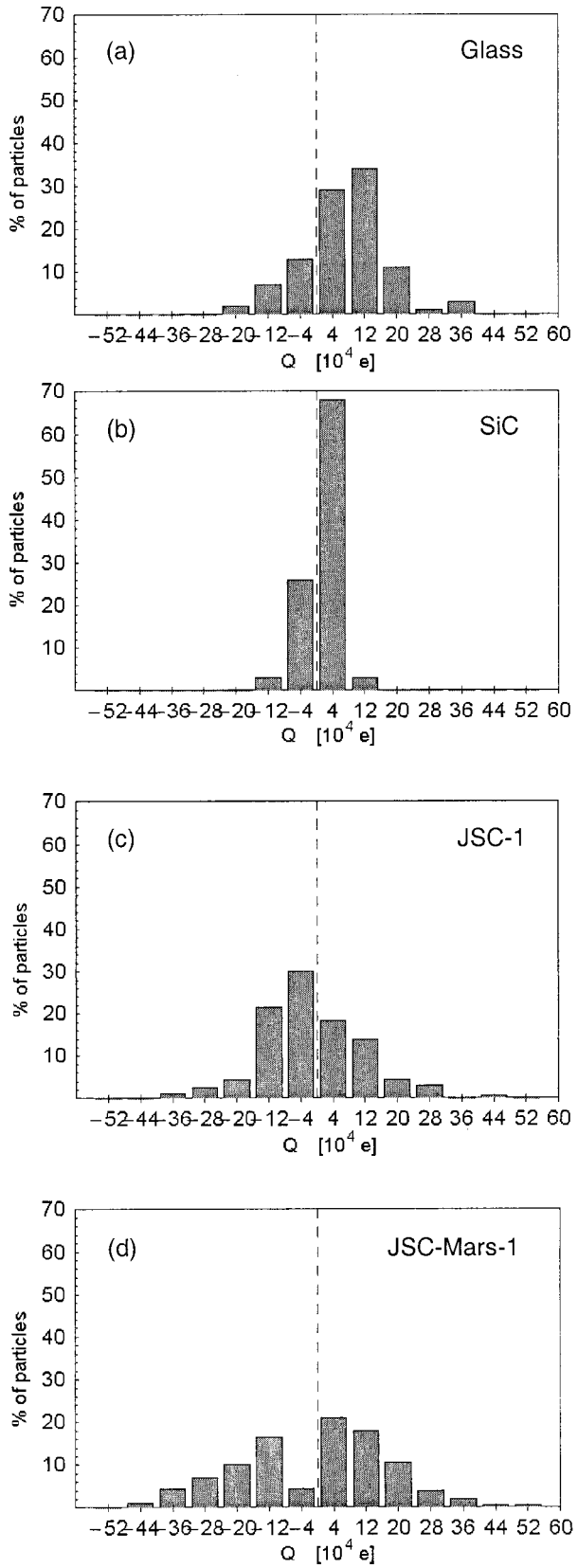

Figure 9. Charge distributions for 100 grains of (a) glass and (b) SiC, and 200 grains of (c) JSC-1 and (d) JSC-Mars-1, where grains were exposed to the arc lamp. The bin size is 8.0×10^4 e, and the dashed line represents zero.

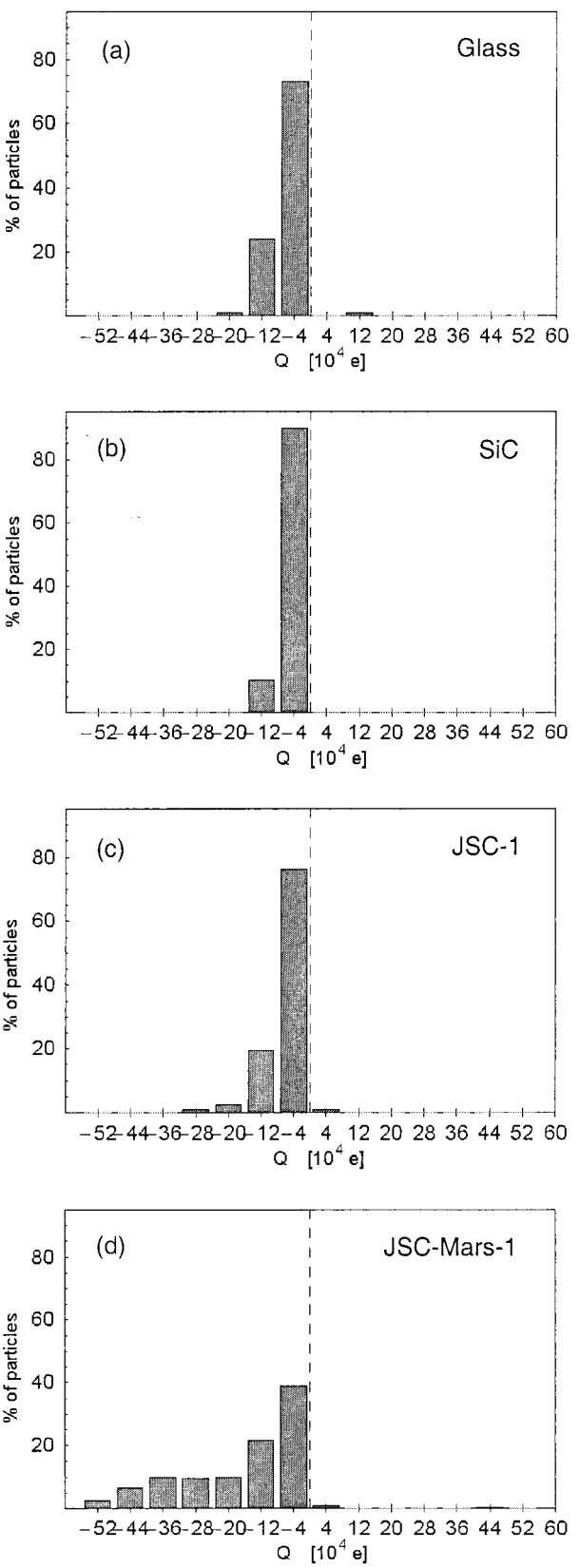

Figure 10. Charge distributions for 100 grains of (a) glass and (b) SiC, and 200 grains of (c) JSC-1 and (d) JSC-Mars-1, where the grains fell through the photoelectron sheath. The bin size is 8.0×10^4 e, and the dashed line represents zero.

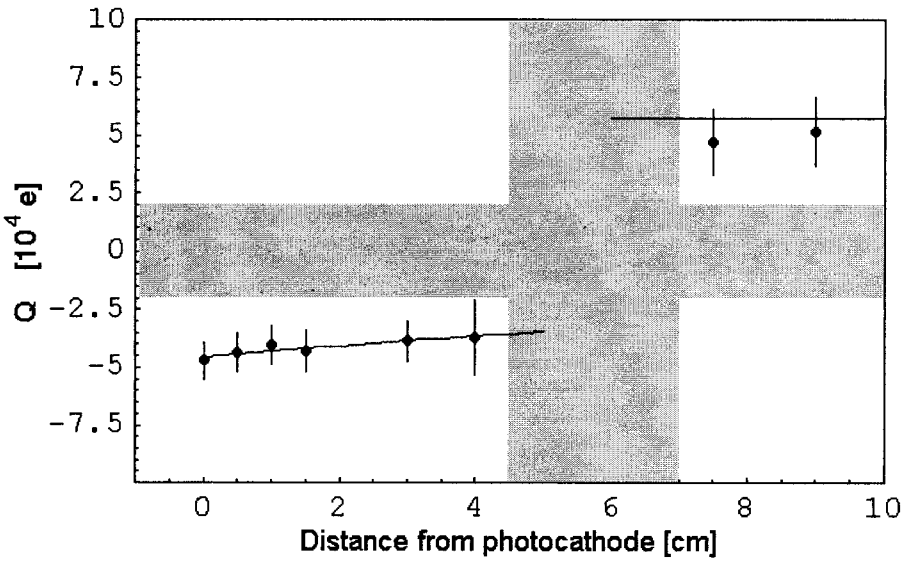

Figure 11. The charge measured on zinc particles having fallen through the sheath as a function of the distance from the photocathode. The horizontal shaded area indicates the detection threshold of $\pm 2 \times 10^4\, e$. The continuous curve on the left indicates the expected theoretical charge using a Maxwellian sheath. The horizontal line on the right indicates the maximum charge on grains due to photoemission and is set by the work function of the zinc particles and the high-energy photon cutoff. Owing to this cutoff, the sheath itself cannot extend to infinity and, as indicated from our charge measurements, the photoelectron density vanishes in the range of 4.5–7 cm from the photocathode. This area is marked by the vertical shaded region.

Equilibrium is reached when this current is equal to the loss of electrons from the particle due to photoemission. Assuming the loss of electrons due to photoemission is constant with distance from the photocathode, $I_g(V, z) = I_g(V) = J_g(V = 0)\pi r_g^2$. The equilibrium condition is thus obtained when $I_s(V, z) = I_g(V, z)$, resulting in an expression for the potential as a function of distance, $V(z)$. The equilibrium charge on a grain as a function of distance from the photocathode is then determined by $Q(z) = CV(z)$. This relationship is plotted as a continuous curve on the left side of Figure 11. The results show an excellent agreement between the measurements and this model with $\lambda_e = 4$ cm.

For particles outside of the sheath the maximum equilibrium potential is determined by the high-energy cutoff of the photons. The solid line on the right side of Figure 11 corresponds to this potential, $V(z \gtrsim 6\text{ cm}) = (hc/\lambda_{\min} - \phi_{\text{Zn}}) = 1.70$ V $(5.8 \times 10^4\, e)$. For $z \gtrsim 6$ cm the measured positive charges are close to the theoretical maximum, indicating that the electron density from the sheath is much below the value expected from a Maxwellian velocity distribution. We interpret this as a sign of the finite extent of the photoelectron sheath, due to the lack of emitted electrons with energies above the cutoff. The finite extent of a sheath for electrons with a monodisperse or rectangular initial velocity distribution is well understood [*Grard and Tunaley*, 1971], and it is not surprising for our case, which is similar to a truncated Maxwellian.

5. Discussion

Experiments performed on the photoelectric charging of isolated conducting dust particles agree well with theoretical models. Conducting particles exposed to ultraviolet illumination attain a positive floating potential due to photoemission, as is expected for grains in interplanetary space. For grains exposed to the solar spectrum, calculation of the charge requires integration over the photoelectron spectrum as described by *Willis et al*. [1973]. Using the work functions of the particles and short-wavelength cutoff of the arc lamp, we verify that (1) provides an accurate calculation of the charge due to photoemission on isolated grains in our experiment.

For dust released from the surface of the Moon or other photoemitting bodies, it has been suggested that the charging currents for the grain are dominated by the collection of electrons from the photoelectron sheath. Our experiments support this model, since isolated conducting grains attain a negative potential of a few volts after passing through the photoelectron sheath. The measured charges are approximately those calculated by equating the electron collection current from the sheath, given by (7), to the photoemission current.

The change in sign of the equilibrium charge on a conducting grain with distance from the photocathode, Figure 11, provides an important confirmation of the theoretical models for the lunar horizon glow. These data demonstrate that a particle is positively charged when it is sufficiently far from the surface for the collection of sheath electrons to be reduced. Since the electric field in the lunar photoelectron sheath points upward, the force on positive particles balances gravitational forces, and these grains can be levitated. In the experiment, particles attain a positive charge at a distance just beyond the screening distance of the photoelectron sheath. Similarly, the observed elevation of the lunar glow is of the same order as the sheath thickness calculated from the emission rates measured for lunar material [*Willis et al*., 1973]. Unlike the Moon, atmospheric transport of particulates is important on Mars. In the absence of strong winds, however, a similar phenomenon with a similar scale height could operate on Mars, particularly at the high altitudes and low atmospheric pressures of the Tharsis volcanoes. In the absence of extreme and rapidly varying horizontal electric fields, electrostatic levitation of dust grains on

Mars, like aeolian transport, requires some other process to break the interparticle surface forces [*Greeley et al*., 1992].

Experiments with nonconducting particles reveal significant triboelectric charging. Unlike the conducting grains, these particles are weak photoemitters. When exposed to UV illumination, particles which initially have an excess of electrons photoemit. Initially positive particles remain unchanged. After falling through the photoelectron sheath, all particles have a negative floating potential. This is expected, since particles with an initially positive charge will gain electrons from the sheath while initially negative particles will remain negatively charged.

The detection of significant triboelectric charging on the nonconducting particles requires reconsideration of the charging of dusty objects, as this process is usually omitted from models. The observed level of the triboelectric charging potential is much greater than the charging potential from the photoelectric processes (up to ± 15 V compared with ± 1 to 2 V). The presence of a photoelectron sheath above a surface provides an electron current, resulting in an increased electrical conductivity at the surface. The sheath electrons will tend to make the surface potential uniform; thus the triboelectric potential may be reduced for illuminated surfaces. For bodies with UV-absorbing atmospheres or for surfaces that face away from the Sun for long intervals, however, triboelectric charging may be the dominant charging process. Dust particles exposed to wind, such as on the surface of Mars, are particularly susceptible to triboelectric charging, because the fraction of the surface which is charged is increased by multiple contacts. This theory is supported by the detection of electrical discharges in agitated Martian regolith simulant [*Fábian et al*., 2001].

In addition, triboelectric charging may act as a mechanism to assist in the formation of a layer of levitated grains. The equilibrium charge on a grain is negative near the photoemitting surface, which can prevent grains from reaching the altitude where the equilibrium charge would be positive. However, grains released by an impact or disturbance can have a positive triboelectric charge, and their motion may be sufficiently rapid to allow transport to a few shielding distances from the surface without becoming negatively charged. Particles that bounce on the surface may also attain a triboelectric charge that is different from the local equilibrium charge. Such processes may also be active on the dusty surfaces of asteroids and small planetary satellites.

Further experiments will explore the stable equilibrium positions for dust grains in a photoelectron sheath and the dynamics of such levitated particles. Additional experiments also include the charging of grains at rest on a surface when there is an electric field above the surface.

Acknowledgments. The authors acknowledge support from NASA (NAG3-2136) and the Department of Energy (Fusion Energy Sciences). We thank Matt Triplett and Zoltan Sternovsky for their assistance, and Bob Walch for initial development of the apparatus.

Janet G. Luhmann thanks D. Asoka Mendis and another referee for their assistance in evaluating this paper.

References

Allen, C. C., K. M. Jager, R. V. Morris, D. J. Lindstrom, M. M. Lindstrom, and J. P. Lockwood, Martian soil simulant available for scientific, educational study, *Eos Trans. AGU*, *79*(34), 405, 1998.

Anderson, R., S. Bjornson, D. C. Blanchard, S. Gathman, J. Hughes, S. Jonasson, C. B. Moore, H. J. Survilas, and B. Vonnegut, Electricity in volcanic clouds, *Science*, *148*, 1179–1189, 1965.

Berg, O. E., H. Wolf, and J. Rhee, Lunar soil movement registered by the Apollo 17 cosmic dust experiment, in *Interplanetary Dust and Zodical Light*, pp. 233–237, Springer-Verlag, New York, 1975.

Burns, J. A., M. R. Showalter, D. P. Hamilton, P. D. Nicholson, I. De Pater, M. E. Ocert-Bell, and P. C. Thomas, The formation of Jupiter's faint rings, *Science*, *284*, 1146–1150, 1999.

Colwell, J. E., and L. W. Esposito, A model of dust production in the Neptune ring system, *Geophys. Res. Lett*., *17*, 1741–1744, 1990a.

Colwell, J. E., and L. W. Esposito, A numerical model of the Uranian dust rings, *Icarus*, *86*, 530–560, 1990b.

Diebold, D., N. Hershkowitz, A. D. Bailey III, M. H. Cho, and T. Intrator, Emissive probe current bias method of measuring dc vacuum potential, *Rev. Sci. Instrum*., *59*(2), 270–275, 1988.

Doe, S. J., O. Burns, D. Pettit, J. Blacic, and P. W. Keaton, The levitation of lunar dust via electrostatic forces, in *Engineering, Construction, and Operations in Space*, pp. 907–915, Am. Soc. Civil Eng., New York, 1994.

Fábian, A., C. Krauss, A. Sickafoose, M. Horányi, and S. Robertson, Measurements of electrical discharges in Martian regolith simulant, *IEEE Trans. Plasma Sci*., in press, 2001.

Farrell, W. M., M. L. Kaiser, M. D. Desch, J. G. Houser, S. A. Cummer, D. M. Wilt, and G. A. Landis, Detecting electrical activity from Martian dust storms, *J. Geophys. Res*., *104*, 3795–3801, 1999.

Feuerbacher, B., and B. Fitton, Experimental investigation of photoemission from satellite surface materials, *J. Appl. Phys*., *43*(4), 1563–1572, 1972.

Freier, G. D., The electric field of a large dust devil, *J. Geophys. Res*., *65*, 3504, 1960.

Gilbert, J. S., S. J. Lane, R. S. J. Sparks, and T. Koyaguchi, Charge measurements on particle fallout from a volcanic plume, *Nature*, *349*, 598–600, 1991.

Goertz, C. K., Dusty plasmas in the solar system, *Rev. Geophys*., *27*(2), 271–292, 1989.

Grard, R., Solar photon interaction with the Martian surface and related electrical and chemical phenomena, *Icarus*, *114*, 130–138, 1995.

Grard, R. J. L., and J. K. E. Tunaley, Photoelectron sheath near a planetary probe in interplanetary space, *J. Geophys. Res*., *76*, 2498–2505, 1971.

Greeley, R., N. Lancaster, S. Lee, and P. Thomas, Martian aeolian processes, sediments, and features, in *Mars*, edited by H. H. Kieffer et al., pp. 730–766, Univ. of Ariz. Press, Tucson, 1992.

Harper, W. R., How do solid surfaces become charged?, in *Static Electrification*, *IOP Conf. Ser*., *4*, p. 3, Inst. of Phys., London, 1967.

Horányi, M., J. A. Burns, and D. P. Hamilton, The dynamics of Saturn's E Ring particles, *Icarus*, *97*, 248–259, 1992.

Horányi, M., B. Walch, S. Robertson, and D. Alexander, Electrostatic charging properties of Apollo 17 lunar dust, *J. Geophys. Res*., *103*, 8575–8580, 1998.

Ip, W. H., Electrostatic charging and dust transport at Mercury's surface, *Geophys. Res. Lett*., *13*, 1133–1136, 1986.

Lee, P., Dust levitation on asteroids, *Icarus*, *124*, 181–194, 1996.

Lowell, J., and A. C. Rose-Innes, Contact electrification, *Adv. Phys*., *29*, 947–1023, 1980.

McKay, D. S., J. L. Carter, W. W. Boles, C. C. Allen, and J. H. Alton, JSC-1: A new lunar soil simulant, in *Engineering, Construction, and Operations in Space IV*, pp. 857–866, Am. Soc. of Civ. Eng., New York, 1994.

Melnik, O., and M. Parrot, Electrostatic discharge in Martian dust storms, *J. Geophys. Res*., *103*, 29,107–29,117, 1998.

Mendis, D. A., and M. Rosenberg, Cosmic dusty plasma, *Annu. Rev. Astron. Astrophys*., *32*, 419–463, 1994.

Mendis, D. A., J. R. Hill, H. L. F. Houpis, and E. C. Whipple Jr., On the electrostatic charging of the cometary nucleus, *Astrophys. J*., *249*, 787–797, 1981.

Michaelson, H. B., The work function of the elements and its periodicity, *J. Appl. Phys*., *48*(11), 4729–4733, 1977.

Nitter, T., and O. Havnes, Dynamics of dust in a plasma sheath and injection of dust into the plasma sheath about moon and asteroid surfaces, *Earth Moon Planets*, *56*, 7–34, 1992.

Nitter, T., O. Havnes, and F. Melandsø, Levitation and dynamics of charged dust in the photoelectron sheath above surfaces in space, *J. Geophys. Res*., *103*, 6605–6620, 1998.

Pelizzari, M. A., and D. R. Criswell, Lunar dust transport by photo-

electric charging at sunset, *Proc. Lunar Planet. Sci. Conf. 9th*, *3*, 3225–3237, 1978.
Reasoner, D. L., and W. J. Burke, Measurement of the lunar photoelectron layer in the geomagnetic tail, in *Photon and Particle Interaction With Surfaces in Space*, edited by R. J. L. Grard, pp. 369–387, D. Reidel, Norwell, Mass., 1973.
Rennilson, J. J., and D. R. Criswell, Surveyor observations of lunar horizon glow, *The Moon*, *10*, 121–142, 1974.
Robertson, S., Experimental studies of charged dust particles, *Phys. Plasmas*, *2*, 2200–2206, 1995.
Rosenberg, M., D. A. Mendis, and D. P. Sheehan, UV-induced coulomb crystallization of dust grains in high pressure gas, *IEEE Trans. Plasma Sci*., *24*, 1422–1429, 1996.
Showalter, M. R., and J. N. Cuzzi, Seeing ghosts: Photometry of Saturn's G Ring, *Icarus*, *103*, 124–143, 1993.
Sickafoose, A. A., J. E. Colwell, M. Horányi, and S. Robertson, Photoelectric charging of dust particles in vacuum, *Phys. Rev. Lett*., *84*, 6034–6037, 2000.
Singer, S. F., and E. H. Walker, Photoelectric screening of bodies in interplanetary space, *Icarus*, *1*, 7–12, 1962a.
Singer, S. F., and E. H. Walker, Electrostatic dust transport on the lunar surface, *Icarus*, *1*, 112–120, 1962b.
Suits, C. G. (Ed.), *The Collected Works of Irving Langmuir*, vol. 3, Pergamon, Tarrytown, N. Y., 1961a.
Suits, C. G. (Ed.), *The Collected Works of Irving Langmuir*, vol. 4, Pergamon, Tarrytown, N. Y., 1961b.
Verboncoeur, J. P., A. B. Langdon, and N. T. Gladd, An object-oriented electromagnetic PIC code, *Comput. Phys. Commun*., *87*, 199–211, 1995.
Walbridge, E., Lunar photoelectron layer, *J. Geophys. Res*., *78*, 3668–3687, 1973.
Walch, R. A., M. Horányi, and S. Robertson, Measurement of the charging of individual dust grains in a plasma, *IEEE Trans. Plasma Sci*., *22*, 97–102, 1994.
Walch, B., M. Horányi, and S. Robertson, Charging of dust grains in plasma with energetic electrons, *Phys. Rev. Lett*., *75*, 838–841, 1995.
Willis, R. F., M. Anderegg, B. Feuerbacher, and B. Fitton, Photoemission and secondary electron emission from lunar surface material, in *Photon and Particle Interaction With Surfaces in Space*, edited by R. J. L. Grard, pp. 369–387, D. Reidel, Norwell, Mass., 1973.
Wood, D. M., Classical size dependence of the work function of small metallic spheres, *Phys. Rev. Lett*., *46*, 749, 1981.
Zook, H. A., and J. E. McCoy, Large-scale lunar horizon glow and a high altitude lunar dust exosphere, *Geophys. Res. Lett*., *18*, 2117–2120, 1991.
Zook, H. A., A. E. Potter, and B. L. Cooper, The lunar dust exosphere and Clementine lunar horizon glow, *Lunar Planet. Sci. Conf*., *26*, 1577–1578, 1995.

J. E. Colwell, M. Horányi, S. Robertson, and A. A. Sickafoose, Laboratory for Atmospheric and Space Physics, University of Colorado, Boulder, CO 80309-0392. (amanda@casper.colorado.edu)

(Received September 20, 2000; revised November 14, 2000;
accepted December 11, 2000.)